



Contents lists available at ScienceDirect

# International Journal of Rock Mechanics & Mining Sciences

journal homepage: [www.elsevier.com/locate/ijrmms](http://www.elsevier.com/locate/ijrmms)

## Technical Note

# A new apparatus and methodology for hydromechanical testing and geometry scanning of a rock fracture under low normal stress



Johan Thörn\*, Åsa Fransson

Division of GeoEngineering, Department of Civil and Environmental Engineering, Chalmers University of Technology, SE-412 96 Gothenburg, Sweden

## ARTICLE INFO

### Article history:

Received 25 February 2015

Received in revised form

3 July 2015

Accepted 19 August 2015

### Keywords:

Rock fracture

Fracture aperture

Stereo photogrammetry

Hydromechanical coupling

## 1. Introduction

Fractures conduct most of the groundwater in hard crystalline rock. The ability of each fracture to transmit water depends on the void space between the fracture surfaces. The geometry of these surfaces is the result of the current stress situation, the manner in which the fracture was formed and subsequent movements, stresses and infillings. This results in a system that is difficult to describe in a way that is both hydraulically and mechanically sound. Such descriptions are useful though, for example in multiphysics modelling for advanced underground constructions, such as repositories for underground storage of nuclear waste.

The cubic law<sup>1</sup> represents the fracture surfaces as two smooth parallel plates without any contact, which is useful for describing the flow of water through the fracture.<sup>2</sup> However, the cubic law is not sufficient to describe the interaction of stresses across the fracture as this would require an understanding of the roughness of, and contact between the surfaces. Key aspects of a fracture that will be accounted for in this work is the hydraulic aperture of the fracture,  $b$  and number of contact points and contact area. The aperture being related to the pore volume and the ability of the fracture to transmit water and the contacts being related to the transference of stresses.

The aim of the work presented here was to develop an

experimental method and the necessary equipment to produce a coupled hydromechanical and surface geometry description of fracture samples with the intention to capture aperture and distance between contact points, here suggested to be approximated by its correlation length. The correlation length is assumed to give an indication of the distance between contact points and to give further insight into the aspect ratio of the voids (i.e. contact point distance divided by aperture). The laboratory experiment also aimed at investigating the validity of the aperture–stiffness relationship derived from the basic model in<sup>3</sup> and the related field data analyses and assumptions: a fracture of low compressive stress across, and limited prior deformation. Focus in this experiment is on fracture normal deformation rather than shear.

A situation with low confining stresses can be expected at shallow depths in bedrock but also at certain locations and in certain directions in the vicinity of an underground opening, where the stress situation is disturbed by the opening. In most cases, previous work involving hydromechanical laboratory experiments on rock cores did not aim at describing the situation in an excavation damage zone (EDZ) close to an underground opening with the presence of stress redistributions and loosened rock.

Tatone and Grasselli<sup>4</sup> presented a method for scanning the geometry of the fracture surfaces and their interrelationship and hence the void geometry of fractures. We present a similar fracture void scanning method, but with samples under predetermined compressive stress. This is an extension of the setup and procedure we used for previous hydromechanical experiments on the same core samples, which included hydraulic testing and deformation measurements across the fracture in the samples.<sup>5</sup>

\* Corresponding author.

E-mail addresses: [johan.thorn@chalmers.se](mailto:johan.thorn@chalmers.se) (J. Thörn), [asa.fransson@chalmers.se](mailto:asa.fransson@chalmers.se) (Å. Fransson).

The working hypothesis was that a carefully designed surface scanning procedure allows the fracture void geometry to be mapped, enabling a comparison to be made between the calculation of the hydraulic apertures in the samples using cubic law and a geometry-based hydraulic aperture calculation, such as the one presented by Zimmerman and Bodvarsson.<sup>6</sup> Experimental testing of the agreement between the previously suggested stiffness to hydraulic aperture relationship<sup>3,7</sup> and the results from this experiment is conducted on the assumption that the results would fall into line with the stiffness to hydraulic aperture relationship in Refs. 3,7. With this comparison both in situ and laboratory scale is included, but apart from that the issue of upscaling is left for coming studies.

Three samples were scanned and analysed in this study. The samples were core drilled from slabs sawn from tunnel walls at the Åspö Hard Rock Laboratory, Oskarshamn, Sweden. The samples have undergone permeameter testing<sup>8</sup> and a subsequent re-run using updated equipment and focus on hydromechanical testing.<sup>5</sup>

## 2. Theory

### 2.1. Fracture apertures

A common understanding of the flow in fractures is that it can be compared to the flow between two smooth parallel plates: the cubic law.<sup>1</sup> The applicability to rock fractures has been investigated and in general the description holds good for smooth, wide aperture fractures with low flow rates.<sup>2</sup> The cubic law includes the hydraulic aperture  $b$  [μm], the transmissivity of the fracture  $T$  [m<sup>2</sup>/s], the viscosity  $\mu_w$  [Pa s], the density of water  $\rho_w$  [kg/m<sup>3</sup>] and the acceleration due to gravity  $g$  [m/s<sup>2</sup>]:

$$b = \sqrt[3]{\frac{12\mu_w T}{\rho_w g}} \quad (1)$$

A more general description of hydraulic aperture and its relationship to the mechanical aperture and surface appearance has been sought empirically<sup>9</sup> and analytically.<sup>6</sup> Zimmerman and Bodvarsson<sup>6</sup> present a relationship that involves the hydraulic aperture  $b$  [μm], the arithmetic mean of the mechanical aperture  $a$  [μm], its standard deviation  $\sigma$  [μm] and the proportion of contact area of the surfaces  $c$  [dimensionless]:

$$b^3 = \langle a \rangle^3 \left[ 1 - \frac{1.5\sigma_a^2}{\langle a \rangle^2} \right] (1 - 2c) \quad (2)$$

For larger values of standard deviation the expression within square brackets in Eq. (2) becomes negative and the result unrealistic. An alternative expression that handles large standard deviations better is<sup>10,11</sup>:

$$b^3 = \langle a \rangle^3 \left[ 1 + \frac{\sigma_a^2}{\langle a \rangle^2} \right]^{-3/2} \quad (3)$$

If the fracture aperture distribution is lognormal, as was found in Refs. 12–15, the geometric mean of the aperture is a very good approximation of the hydraulic aperture.<sup>16</sup> However, describing the data by means of a statistical distribution does not capture the void space entirely. Hakami and Larsson<sup>17</sup> include the spatial variation by conducting a variogram analysis, thus establishing a correlation length of the aperture variation.

An empirical relationship using data from hydraulic interference tests, including data from the same area as the samples in this study,<sup>18</sup> links the transmissivity and storativity of fractures:

$$S = 0.0109T^{0.71} \quad (4)$$

A link between fracture stiffness and storativity<sup>19</sup> is achieved as once the negligible influence of the compressibility of water is removed from the expression:

$$k_n = \frac{\rho_w g}{S} \quad (5)$$

Together with the cubic law, Eq. (1), linking transmissivity and aperture, an estimate of fracture stiffness from an in situ hydraulic test is reached which depends on the properties of the injected water (density, viscosity), gravity and the hydraulic aperture of the fracture. This relationship is assumed to capture the fracture that is least stiff and most transmissive in a tested interval:

$$k_n = \rho_f g \left[ 0.0109 \left( \frac{\rho_f g b_h^3}{12\mu} \right)^{0.71} \right]^{-1} \quad (6)$$

In Ref. 3, a basic conceptual model of fracture contact distances resulted in a link between stiffness and aperture on the form

$$k_n \approx Cb^{-2} \quad (7)$$

Both Eqs. (6) and (7) include estimates of fracture stiffness being inversely proportional to hydraulic aperture squared,  $b^{-2}$ , but achieved from hydraulic and geometrical concepts, respectively:

### 2.2. Measurement of fracture aperture

Surface geometry and/or aperture have been studied for a long time, with different approaches used for the measurement and under different boundary conditions. Tatone and Grasselli<sup>4</sup> provide an account of methods published over four decades.

When the surface geometry of a fracture is measured, a common definition of aperture is the difference in the z-coordinate when a best-fit plane of the fracture is aligned with the x–y plane (Eq. (1)).<sup>4,11,20</sup> This is used because of its computational simplicity but results in overestimated apertures, especially for rough surfaces<sup>21</sup>:

$$a(x, y) = z_2(x, y) - z_1(x, y) \quad (8)$$

Methods that attempt to measure the fracture aperture include rubber injection into a fracture sample with subsequent measurement of rubber thickness by photographing the cast with a light source underneath.<sup>22</sup> In this case, the position between the fracture sides was established by placing one half on top of the other, with the stress across the fracture resulting from the weight of the overlying part. Other injection approaches has been utilised in e.g. Refs. 13,14 with the possibility of determining the aperture under specific stress across the fracture, but with impractical and/or low resolution aperture data acquisition, through slicing the sample and digitising the cross sections.

Laser profilometry scanning of fracture surfaces with stereophotographic data collection was used in Ref. 21 where the aperture, under the stress resulting from the weight of the overlying sample part. Here the aperture was determined by means of referenced data collection with spheres on the sample halves.

Another recent approach to optical profilometry with white light used a special jig to fit the sample halves.<sup>20</sup> This approach helped to determine accurately how each surface characterisation could be combined to obtain an aperture but it did not allow for measuring the aperture situation under stress.

The method in Ref. 4 included measurement using an optical measurement system named ATOS, which was used on a fractured rock core sample by first establishing the spatial interrelationship between the core pieces and then scanning the fracture surfaces. When using this method, the core pieces were placed in a best-fit position and clamped before determining their relative positions and surface geometry measurement. The clamping stress was however unknown.

From the mentioned studies,<sup>4,13,14,20–22</sup> we identified the lack of a combined hydraulic and mechanical testing procedure with high resolution, handy scanning of surface geometry and aperture at a predetermined stress level that is in the same range as the hydromechanical testing procedure.

### 3. Measurement method

The experimental method include sampling of a natural fracture, testing that fracture sample in a permeameter, scanning the fracture surfaces and combining the resulting pair of surface topographies into an aperture map. The following steps were taken (as outlined in Fig. 1): (a) slabs were sawn from the walls of the TASS and TASQ tunnels at Äspö HRL. (b) A steel plate was bolted across a selected fracture, and a 190 mm cylindrical sample drilled. (c) The sample was tested in permeameter after removing the steel plate, giving hydraulic flow and mechanical deformation at four load cycles. The sample was then place in a modified cell (d) where the distance between the sample halves at 1.0 MPa confining pressure was established. Thereafter the fracture surfaces were scanned (e), enabling an aperture map generated in the coordinate system from step (d). The cylindrical fracture samples were held in place with circumferential rubber bands from that the drilling aid steel plate were removed, until opening the fracture for scanning (from (b) to (d) in Fig. 1), thus essentially keeping the halves in correct relative positions. As a consequence, this approach of keeping the sample halves together was in conflict to determining the mechanical initial aperture, before the permeameter testing. The scanned aperture is then essentially the result of a fifth load “cycle” of 1.0 MPa, carried out after remounting the sample into a modified cell.

#### 3.1. Sampling

The TASS tunnel at Äspö HRL was built for demonstrating fine sealing of tunnels at great depth (450 m).<sup>23</sup> Careful blasting, minimising the excavation damage zone (EDZ) was a part of the procedure. After completion investigations on the extent and characteristics of the EDZ were carried out.<sup>8,24,25</sup> A part of the EDZ investigations was to saw blocks from the wall of the TASS tunnel and another tunnel called TASQ (cf. “a” in Fig. 1). The blocks from TASS were sliced into 75 slabs of roughly 1.5 m × 0.5 m × 0.1 m, and natural and blast fractures were mapped on the surfaces of the slabs.

Twenty samples were drilled from the slabs for use in permeameter experiments (cf. “b and c” in Fig. 1), as reported in Ref. 8. Sampling was done by bolting a steel plate across the fracture

trace, and core drilling around the plate (190 mm diameter), thus keeping the halves of the cylinders in place, avoiding wear of the surfaces originating from the drilling procedure. The sampling positions were chosen in such a way that one fracture would cut through the centre of each sample.

#### 3.2. Hydromechanical permeameter measurements

The procedure and results from stepwise hydromechanical permeameter experiments on four samples was reported in Ref. 5, with a step-by-step account of the method in Ref. 26.

The permeameter consists of a stainless steel cell (see schematic representation of the experimental set-up in Fig. 2 and a cutaway photo montage of the cell in Fig. 3), where isotropic pressure could be set up to 2.5 MPa. Water for the flow test was led into the sample from below and collected at the top in a pipe that protruded from the cell. A deformation sensor was mounted in plastic brackets, which were epoxy-glued to the sample, perpendicular to the fracture trace in the centre of the top surface of the core. The sensor and brackets were housed in a milled hole in the lid. A Microstrain DVRT<sup>®</sup> with a stroke of 3 mm and resolution of 1.5 μm was used for deformation measurements ( $\Delta a$ ) across the fractures.

The internal fluid pressure loss across the sample is denoted  $dh$ , and was measured using a sensor placed at the same height as the outflow from the cell. In the experimental set-up,  $dh$  was defined as the height difference between the water table in the supply container and the outflow from the cell. The value of  $dh$  was kept constant at 0.6 m mainly by raising the container at the same rate that the water level in the container decreased. A secondary solution, used for the samples with small apertures, was to apply compressed air in the supply container ( $dh=35$  m) (see Fig. 2).

To mount a core sample in the cell (Fig. 3), it was placed on the steel base. The displacement sensor was fitted into the brackets and the steel lid was placed on the sample. Two latex rubber membranes were carefully applied around the sample before the cell casing and lid was bolted in place.

The water storage container was lifted so that the water level in the container and the pressure head remained constant relative to the sample (see Fig. 2) and the  $dh$  pressure head was recorded at a rate of one reading per second and plotted on a screen. Deformation data were also collected at a rate of one reading per second. The flow volume was measured using graded measurement cylinders (100 ml, 50 ml and 20 ml) and Erlenmeyer flasks (10 ml and 2 ml). The time to fill was recorded using a time stamp macro in a Microsoft Excel spreadsheet, running on the same computer as the

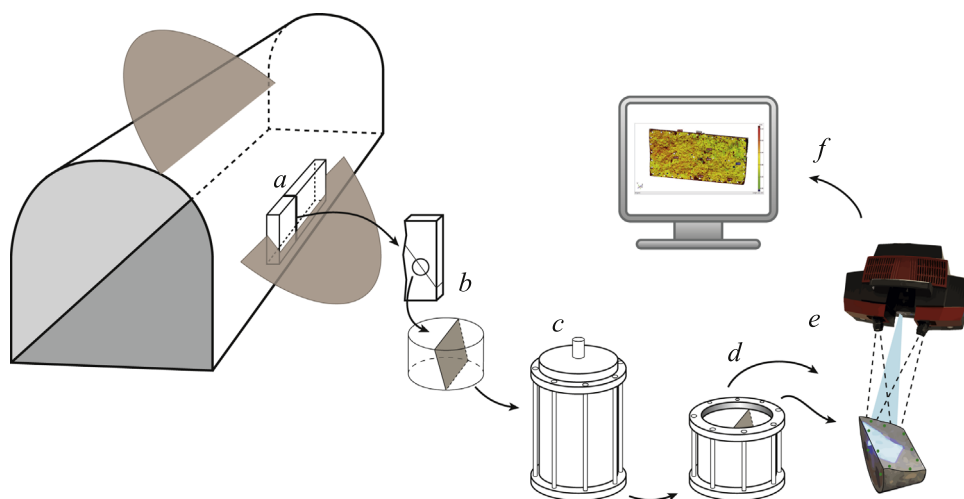
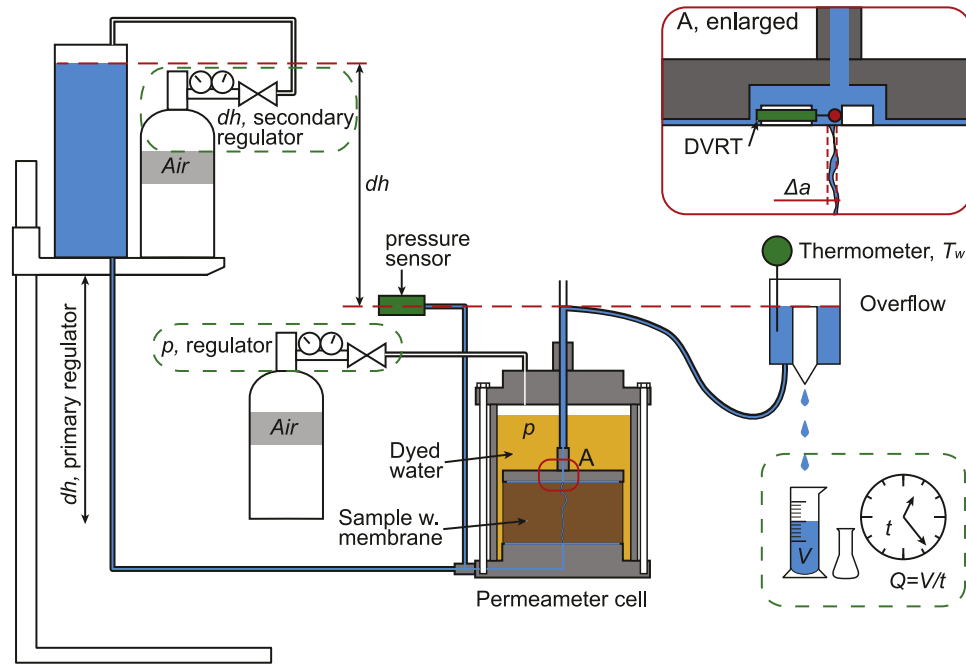


Fig. 1. The steps in the experimental procedure, a–e represent experimental steps as described in Sections 3.1–3.3 and f represent the data processing (Section 3.4).



**Fig. 2.** Sketch of the permeameter set-up. The enlarged part, A, corresponds to the hydromechanical procedure, including mechanical deformation measurement. From Ref. 5, reproduced with permission.

logging software for  $dh$  pressure and  $\Delta a$  deformation, which yielded a synchronised time value for all data sets.

Experiments were conducted stepwise in four cycles of maximum cell pressure (peaking at 1.0, 1.5, 2.0 and 2.5 MPa respectively). For each step the reading of the DVRT transducer was given time to stabilise, and three volume/time flow readings were conducted.

### 3.3. Surface topography scanning

After the permeameter experiments the samples PS0039061, AB1AB2 and PS0039023 were used in the development of the surface scanning method with Tritop<sup>27</sup> and Atos.<sup>28</sup> The concepts of the procedure is found in Fig. 5. The first step (as seen in Figs. 4 and 5a), is to determine the relative positions of the sample halves. This was done by putting the sample in a modified version of the permeameter, where the sample top surface was visible through the lid of the permeameter. The illustration in the top left of Fig. 4 shows the sample and fracture position, with the arrow indicating the flow direction in HM permeameter testing. The cell was then pressurised to 1.0 MPa in order to measure the mechanical aperture in the stress situation of the previously conducted flow experiments.<sup>5,8,26,29</sup> Adhesive code markings (green dots throughout Fig. 5) were put on the top surface and a series of photographs were taken from different angles, and the photographs were analysed automatically by the Tritop/Atos software, generating a 3D model.

After this was done, the core sample was removed from the cell and split. The dots on the upper surface of the sample were supplemented with dots around the edge of the fracture surface. Photographing with Tritop was carried out once again, one core half at a time (Fig. 5b), before scanning the surface geometry of each half using an Atos Triple scan III 3D scanner<sup>28</sup> (Fig. 5c). The dots (that were attached to the sample before photographing to enable a coordinate system to be constructed) were identified using the scanning software, which aligned the scanned surfaces with the coordinate system established in step “a”. The point clouds obtained from the scans were converted into meshes. The meshes of the halves were then compared and a high-resolution

map of the distance between the surfaces, i.e. the mechanical aperture, was obtained (Fig. 5d).

### 3.4. Data processing

Software for the scanning system, GOM Inspect<sup>30</sup> can be used to analyse the surfaces. In this procedure it was used for cropping out the fracture area and exporting the data as pairs of ascii xyz-coordinate files. A Matlab<sup>31</sup> script was written for further data analysis.

The coordinate system in which the scanning occurred was not co-aligned with the average fracture plane, as is a prerequisite for aperture calculation with Eq. (8). Therefore the data processing started with rotating one surface so that the  $xy$ -plane coincided with the average surface plane, and for convenience placing its centre in the origin of the coordinate system. The exact same manipulations were done with the second surface, thus maintaining their relative positions. The needed amount of rotation was established from fitting a plane to one surface, calculating the normal vector of that plane and then conduct a coordinate transform to get the normal vector [0 0 1]. After the rotation procedure the normal vectors to both surfaces were calculated again, and compared to the desired normal vector. The angular differences was less than  $0.8^\circ$ . This is sufficiently close to zero for the aperture estimate of Eq. (8) to be sound. Between the planes the angle was below  $0.1^\circ$ , indicating that the procedure did not cause wedge-shaped apertures.

The aperture calculation was facilitated by interpolating the scattered data on a regular square  $x$ - $y$  grid with 0.06 mm spacing. Point density before interpolation was about 280–320 pts/mm<sup>2</sup> and after interpolation 278 pts/mm<sup>2</sup>. Fig. 6 contains a “to scale” 2D generalisation of the interpolation process.

The effects of different interpolation grid spacings were investigated by comparing the output achieved when using different grid spacings. Spacings of 0.04, 0.05, 0.06, 0.10, 0.15, 0.20 and 0.50 mm were tested. Aperture results were similar for all the tested step lengths but began to differ, mainly in terms of contact area, for the three largest spacings. The calculations presented were conducted using 0.06 mm grid spacing as this rendered a point density close to the original data and maintained reasonable computation time.

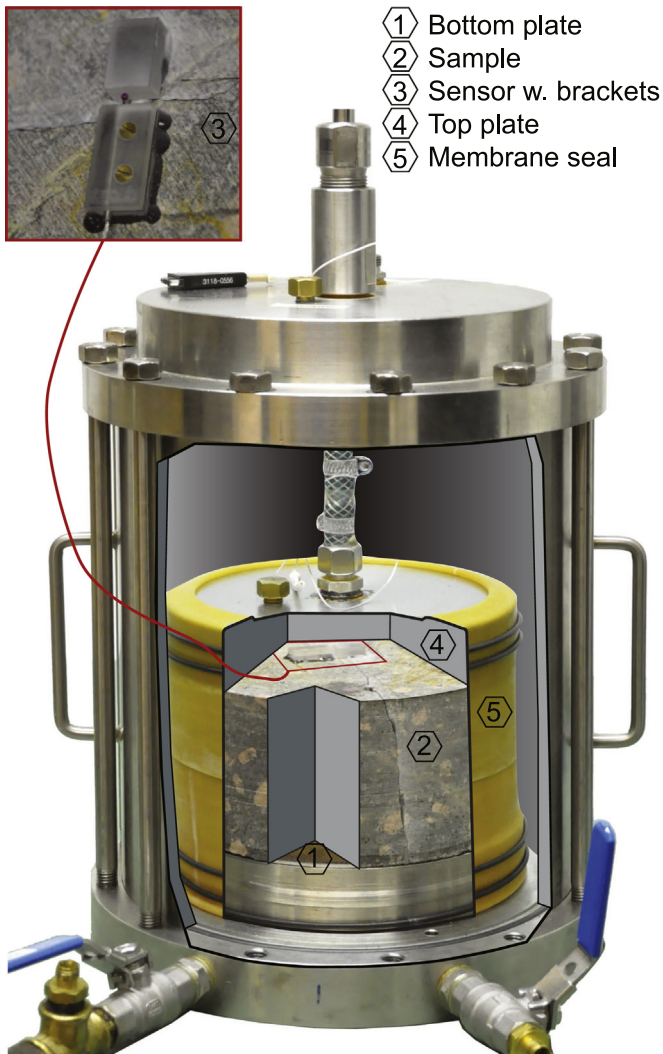


Fig. 3. Cutaway photo montage of the cell with a sample. From Ref. 5, reproduced with permission.

Statistical analysis of the aperture dataset was carried out, as presented in Section 4. The mean, median and standard deviation of the aperture are presented as well as the hydraulic aperture according to Eqs. (2) and (3). For each sample a “global” subsection was used first for analysis. This roughly corresponds to fitting a rectangle 1 cm inside the outer boundaries of the fracture surface. Using this procedure, two types of error data were essentially avoided: firstly the areas where the coordinate dots covered the fracture surface during scanning and secondly the areas around the fracture periphery where the sample preparation probably caused chipping and therefore large apertures. The datasets were also analysed in ten subsections, two rows of rectangles within the global subsection.

Aperture variability was represented by the standard deviations, whilst the spatial correlation, or in-plane void variability, was estimated as the range of an isotropic variogram. The global (G) subsections were used for this analysis and thinned as every tenth value in the  $x$  and  $y$  directions before the range of an isotropic variogram was calculated.

#### 4. Results and discussion

The most important parameters resulting from this study is the layout of the pore space and the consequences for transferring

normal stress and water. This is quantified as hydraulic aperture,  $b$ , the correlation length of the aperture, expressed as the range of a variogram and the contacting surface,  $c$ . These most important parameters are outlined as bold face in the results compilation presented in Table 1. Table 1 also contains numeric values for traceability and validity checks of the data. Further, the estimated hydraulic aperture (and geometric mean) based on surface scanning is compared to estimated hydraulic aperture from permeameter tests (bold face in Table 2). Finally hydraulic aperture from the permeameter tests is related to the estimated normal stiffness from the deformation measurements and compared to a stiffness to aperture relationship suggested from field data (bold face in Table 2 and a compilation in Fig. 10).

##### 4.1. Aperture of scanned samples

The Matlab analysis of the scanning data also resulted in aperture maps, consisting of aperture values onto the 0.06 mm regular grid, and a list of aperture values onto which statistical metrics were calculated. These results are presented in Figs. 7–9 and Table 1. Fig. 7 presents aperture maps of the scanned samples. Each aperture map is supplemented by a (common) key to the subsection numbering, a small map outlining the subsections used for lognormal distribution fitting and a greyscale topography map describing the roughness of one surface rather than the aperture between the surfaces. The colour part includes a 15-step representation of the aperture, where values above and below scale are included in the max/min groups. The greyscale insets illustrate the topography of one surface as a reference to the overall roughness. The aperture presentations in Fig. 7 visualise the differences between the scanned samples. PS0039061 has the largest aperture and least contact area (Table 1), and also the least amount of lost material (resulting in red areas).

In the datasets there are areas of significantly higher aperture, interpreted as missing mineral grains or rock flakes. Sample PS0039023 was split with a light hammer stroke for the first time “ever” between Step a and Step b of the scanning procedure (Fig. 5). Loose flakes were collected and weighed and was found to

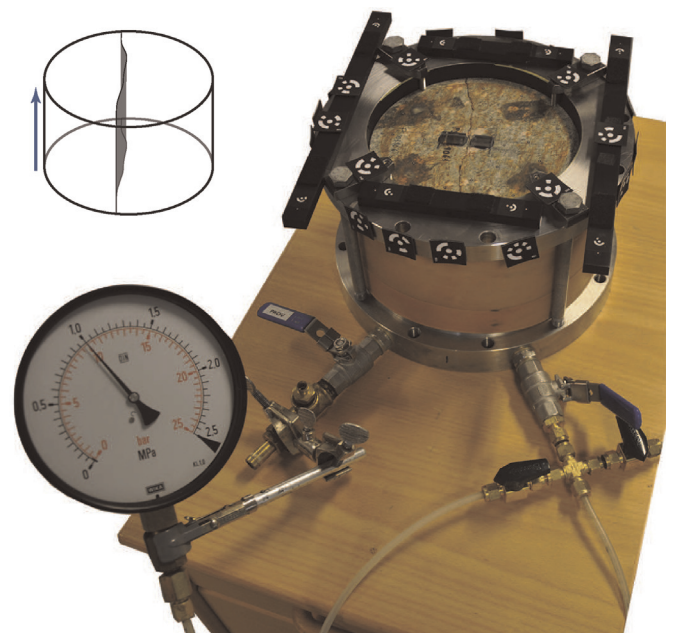
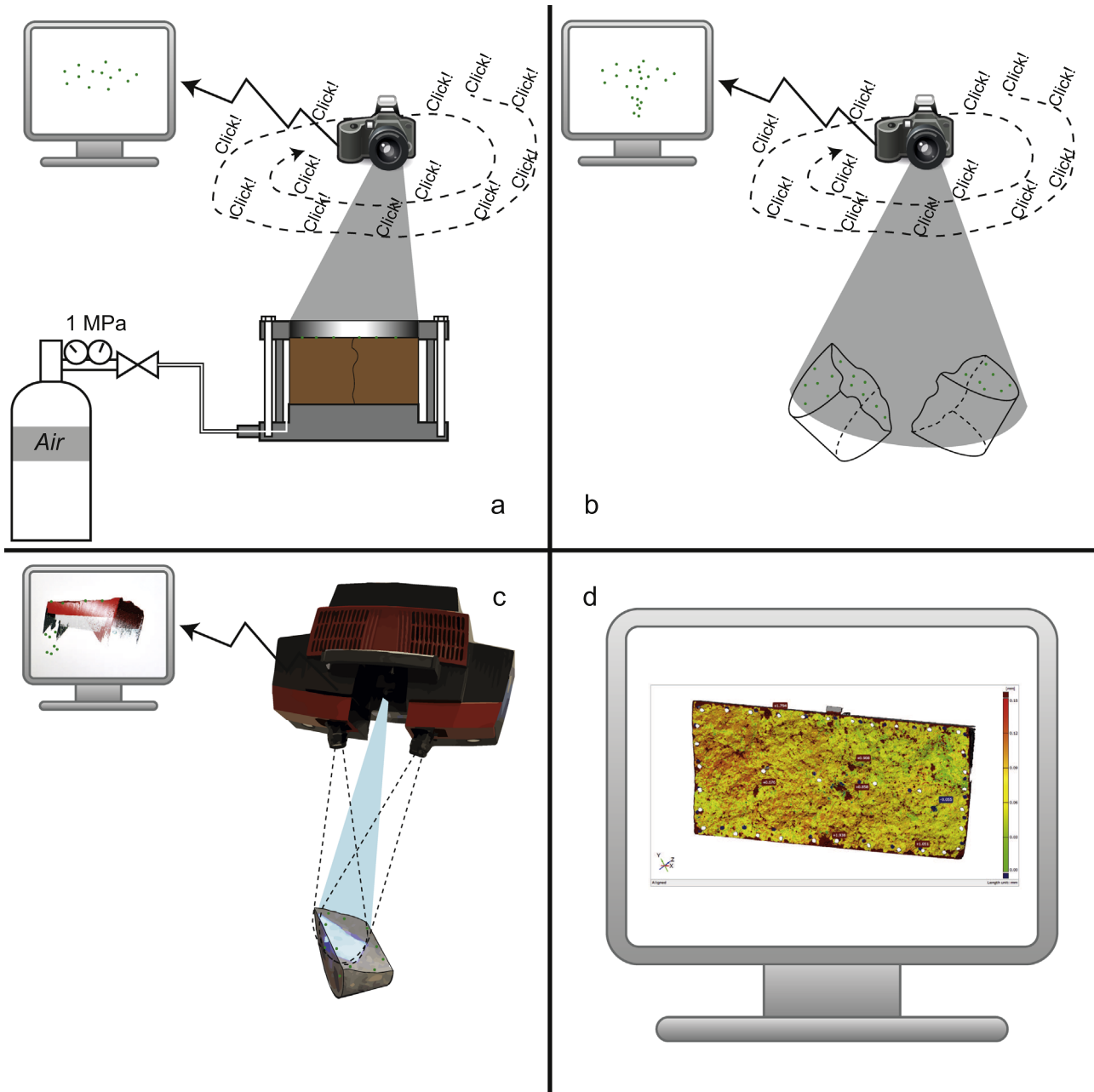


Fig. 4. Sample pressurised to 1.0 MPa with the top surface free, ready for the first step of the scanning sequence. See also Fig. 5 a.



**Fig. 5.** Sequence for scanning and generating a basic aperture map. Steps *a* and *b* captures the relative positions of the fracture halves when under a defined pressure. Step *c*, contain a precise surface scan of the rough topography. In Step *d*, the distances between the points in the scanned halves are calculated, producing an aperture map. Figure from Ref. 35. (For interpretation of the references to colour in this figure, the reader is referred to the web version of this article.)

correspond to a (void) volume of  $0.5 \text{ cm}^3$ . Therefore most of the red areas (high aperture) in Fig. 7 does not reflect the fracture appearance as it was during previous hydromechanical testing. Likewise, some areas of negative aperture can be seen with particularly large areas at AB1AB2. Some of these (including the largest such area, subsections 4 and 9 in Fig. 7) are known to be loose flakes that have not fallen away.

In Fig. 8, point values of apertures from the scanning are presented with 12 numbers for each sample: the ten subsections, G (which is the global section, including all subsections), and S representing the selected subsections as outlined in Fig. 7. Hydraulic aperture,  $b_{hyd}$  is presented as a line for the aperture according to Eq. (3), and supplementary “X” symbols where Eq. (2) produces non-complex values. The problems with using Eq. (2) originates

from high standard deviations in comparison to mean aperture. In terms of coefficient of variation ( $CV = \sigma/b_{mean}$ ) for the groups of selected subsections (S) PS0039061 had a CV of 0.6, AB1AB2 had 1.0 and PS0039023 had 1.6, where the latter two is high in comparison to the compilation in Ref. 32 (Table 1).

Since the geometric mean aperture may, as mentioned previously, be used as hydraulic aperture for lognormal data, the possibility to fit lognormal distributions was checked (Fig. 8 and Table 1). Fitting lognormal distributions directly to aperture data containing fairly large areas of overestimated “lost flake” aperture, as well as underestimated, negative “loose flakes”, is not possible. Consequently, fitting of lognormal distributions was conducted on the subsections which, following visual inspection, had less of these error data (cf. column “G”, global subsections, and “S”,

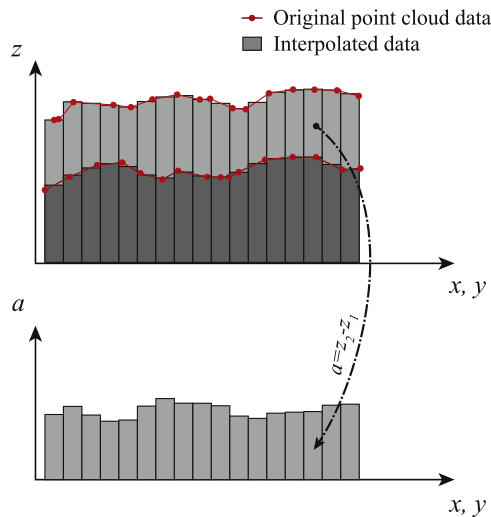


Fig. 6. Interpolation of the data and its representation as a 2D analogue of the actual 3D case. The  $x$ – $y$  axes correspond to the best-fit plane through the entire surface.

selected subsections, in Table 1). A smaller number of negative aperture values were still present and in the case of geometric mean and lognormal distribution fitting they were simply removed from the dataset.

Histograms of the apertures in the selected subsections (S) are found in Fig. 9. For visibility, the total aperture span is set at  $-100$  to  $400 \mu\text{m}$  although the included lognormal distributions are based on the full positive data range. The total amount of data falling outside the histogram window is marked with bars just outside the diagram edges. Lognormal distributions are included in the histograms as red lines. It is evident that the measured distributions are less skewed than the fitted lognormal distributions. The geometric mean values agree with the median values to within 3.5% for the selected subsections (Table 1), which together with the histograms suggest that it is reasonable to assume lognormal distributions for the datasets.

Table 1  
Aperture statistics, global section (G) and the subsections (S); see Fig. 9 for the key to the subsections included in (S). Note: in the equations,  $x$  denotes the single aperture value, representing an area of  $di^2$ ,  $n$  is the number of such elements,  $a$  is the aperture,  $b$  the hydraulic aperture and  $c$  the contact area.

Property	Means of determination	Sample					
		PS0039061		AB1AB2		PS0039023	
		G	S	G	S	G	S
Average aperture [ $\mu\text{m}$ ]	$a_\mu = \frac{1}{n} \sum_{i=1}^n x_i$	100	99.7	70.2	69.3	63.8	49.9
Median aperture [ $\mu\text{m}$ ]	$a_{med} = a_{i=n/2}$	90.5	91.0	57.1	58.8	33.7	37.7
Geometric mean aperture [ $\mu\text{m}$ ]	$a_g = [\prod_{i=1}^n a_i]^{1/n}$ Positive values only	89.8	89.7	56.3	56.8	36.0	36.7
Standard deviation [ $\mu\text{m}$ ]	$\sigma = [\frac{1}{n-1} \sum_{i=1}^n (x_i - \bar{x})^2]^{1/2}$	63.8	58.3	90.8	72.4	236	80.5
Hydraulic aperture [ $\mu\text{m}$ ] Eq. (2)	$b^3 = a_\mu^3 [1 - \frac{1.5\sigma a_\mu^2}{a_g^2} (1 - 2c)]$	73.2	78.5	–	–	–	–
Hydraulic aperture [ $\mu\text{m}$ ] Eq. (3)	$b^3 = \langle a \rangle^3 [1 + \frac{\sigma^2}{\langle a^2 \rangle}]^{-3/2}$	84.5	86.1	43.0	47.9	16.6	26.3
Area in analysis [ $\text{cm}^2$ ]	$A = di^2 \cdot n$	127.6	92.6	153.1	86.6	141.2	71.5
Lognormal $\mu$	Maximum likelihood estimate $a_{\log \mu} = \frac{1}{n} \sum_{i=1}^n \log(x_i)$ Positive values only	–	–2.41	–	–2.87	–	–3.30
Lognormal $\sigma$	Maximum likelihood estimate $\sigma_{\log} = [\frac{1}{n-1} \sum_{i=1}^n (\log(x_i) - \log(\bar{x}))^2]^{1/2}$ Positive values only	–	0.46	–	0.62	–	0.82
Contact [%]	Threshold $1 \mu\text{m}$	0.33	0.07	3.1	0.4	10.3	1.7
Spatial correlation [mm]	Range of isotropic variogram, data thinned to every 100th value ( $10^2$ )	6	–	6	–	12	–

As identified in Ref. 32, contact is a matter of scale. Ideally, contact would show in the measurement results as  $\equiv 0$ . In reality, for any given study contact must be defined as values below a certain threshold that might differ from zero. Even the most noise-free and error-free procedure can be expected to show contact as either small negative or small positive values. When elastic behaviour is added to the contact points, further complexity and local negative aperture values are expected.

When using the smallest measurement volume of the Atos Triple scan III it has an accuracy better than  $0.01 \text{ mm}$  in the surface plane, and at least ten times better out of the plane (in our case aperture). Therefore we saw it reasonable to define contact as apertures less than  $1 \mu\text{m}$ , as was the case in Refs. 32,33.

A third reason for having areas of negative aperture (apart from semi-loose flakes and measurement accuracy) is the elasticity of the contacting asperities. Just as for the semi-loose rock flakes contacting asperities are expected to show some degree of elastic rebound, once the contact stress is released. In this work such asperity deformations are treated globally in the calculation of sample stiffness. Further analysis of the asperity mechanics could be carried out, but was beyond the scope of this study.

The spatial correlation length for the aperture of PS0039061 and AB1AB2 was similar ( $6 \text{ mm}$ ) resulting in a correlation length to aperture ratio of about  $70$ – $100$  (i.e.  $6 \times 10^{-3} / 90 \cdot 10^{-6}$  and  $6 \times 10^{-3} / 60 \cdot 10^{-6}$ ). This is similar to the results reported in Ref. 17, where ranges of  $5$ – $20 \text{ mm}$  were reported for a  $360 \mu\text{m}$  fracture under  $0.45 \text{ MPa}$  load, i.e. correlation length to aperture ratio of  $10$ – $60$ . Further, a preliminary estimated number of contact points (sample size divided by correlation length squared) is similar to the number of contact points counted from the aperture map of sample PS0039061 ( $350$  compared to  $270$  points).

#### 4.2. Comparison with hydromechanical laboratory tests and field data

The scanning results have been compared to the data from permeameter experiments and deformation tests performed on the cores.<sup>5</sup> Table 2 includes the cubic law hydraulic apertures calculated from the deformation across the stress range of different load cycles (e.g. from  $0.25 \text{ MPa}$  to  $1.0$ ;  $1.5$ ;  $2.0$ ;  $2.5 \text{ MPa}$ , see

**Table 2**

Comparison between “scanned apertures” and HM permeameter data: hydraulic apertures calculated in the last 1.0 MPa cell pressure step, with the cubic law from hydromechanical testing and stiffness calculated across the entire pressure range of each cycle.<sup>5,26</sup>

	PS0039061	AB1AB2	PS0039023
<b>Scanned results of selected subsections</b>			
<b>Hydraulic aperture (Eq. (3)) [μm]</b>			
Average aperture ± standard deviation [μm]	86 100 ± 58	48 69 ± 72	26 50 ± 81
Geometric mean aperture [μm]	90	57	37
<b>Permeameter data</b>			
<b>Hydraulic aperture (cubic law) at first and last 1.0 MPa pressure [μm]</b>			
<b>Normal</b>			
stiffness,	Hydraulic, $k_n^b$	92	40
$k_n$ , at cycle	Mechanical,	66	65
peaks	$k_n^a$		100
	Hydraulic, $k_n^b$	64	100
	Mechanical, $k_n^a$	84	220
	Hydraulic, $k_n^b$	–	140
	Mechanical, $k_n^a$		300
	Hydraulic, $k_n^b$	–	160
	Mechanical, $k_n^a$		340
			140

Fig. 10). Furthermore, Table 2 and Fig. 10 present stiffness, calculated as a change in confining pressure (i.e. normal stress) divided by the corresponding aperture change. The tests were conducted as cycles of up to 2.5 MPa, returning to low pressure in between. Stiffness is calculated as the aperture change for the stress change from the low (0.25–0.4 MPa) pressure to the cycle peak pressure. In Fig. 10, the black symbols represent stiffness calculated as a change in hydraulic aperture for a change in confining stress ( $k_n^b$ ). The white symbols are correspondingly measured mechanical deformation for a change in confining stress ( $k_n^a$ ). The solid line correspond to the relation presented in Ref. 3 (Eq. (6)), with dash lines ± one order of magnitude. When comparing the filled symbols of the 1.0 MPa step (i.e. largest aperture) for each sample to apertures calculated with Eq. (3), the correspondence to the line (Eq. (6)), is better than that indicated in Fig. 10 (cf. values in Table 2). A compilation of data from the literature on the same format as Fig. 10 can be found in Refs. 3,7. The fracture tested in Ref. 17, mentioned above, can also be compared to the aperture-stiffness compilation through data in Ref. 34: In Fig.10 these points end up near the upper dashed line.

The mechanical deformation in the permeameter experiments was measured by a single transducer. This leaves any uneven deformation effects unknown. For this study, qualitative estimates of the aperture maps indicate that wedge effects of the apertures did not occur. For coming studies however, the usage of three or more transducers around the sample should be considered. Another future improvement would be to make a rerun in the permeameter after the scanning, to assess the effect of grains falling out when opening the fracture, for example.

The small-aperture fracture PS0039023 is interesting. Since it was partly calcite-sealed when the scanning took place, the general matedness as in the fit between the surfaces from manual handling was as true as is reasonably possible, i.e. the sample halves were kept in place from a–d in Fig. 1.

Fracture PS0039023, having smaller aperture and thus closer to the scanning measurement limit is less confident. In addition, the aperture calculations suffer as a result of the rock grains that fell out when opening the fracture for scanning. Since most grains originate from the area of the global subsection, the average aperture of that section (64 μm) is overestimated by roughly the amount of collected grains (0.5 cm<sup>3</sup> divided by 141.2 cm<sup>2</sup> = 35 μm). This effect accounts for a large part of the discrepancy between the scanned aperture and the hydraulic aperture from HM permeameter tests (for the global subsection, less so for the selected subsections). The same effect is seen in AB1AB2 although to a lesser degree. Another issue with the HM

permeameter testing of PS0039023 is the partial calcite-sealing. Since an unknown proportion of the fracture area did not allow any flow during the permeameter testing, calculating the flow from the entire area results in underestimation of the hydraulic aperture. At the same time, the softer-than-granite calcite filling may underestimate the mechanical stiffness in relation to the proposed field data relationship.

Samples that were tested, even though they are few in number, present a low stiffness for large hydraulic apertures and a high stiffness for small apertures (see Fig. 10 and Table 2). For the field data compilation (solid line), the detailed internal geometry (surface roughness and contact points for mechanical aspects), and the fracture void geometry (hydraulic aspects) were not known. The sample with the smallest hydraulic aperture (PS0039023) shows a difference in stiffness estimated from the change in hydraulic aperture (black symbols) and mechanical deformation (white symbols). This could possibly be due to this fracture reaching a residual hydraulic aperture.

Apart from this, the experimental results and the solid line in Fig. 10 seem to agree fairly well, assuming low compressive stress across fractures with limited prior deformation (e.g. crushing or shearing through of asperities). Shearing, however, has occurred given the fact that at least the two fractures with the largest aperture are not well mated. This suggests that the stress situation (here low compression) and the geometry (contact points and void geometry) are key aspects.

Further identification of the similarities and differences between mechanical and hydromechanical behaviour in relation to actual fracture geometry would most likely produce additional important information and data for both fields.

## 5. Conclusions

Three fracture samples with geometric mean apertures,  $a_g$  of roughly 90, 60 and 40 μm had their surface geometry scanned after hydromechanical permeameter experiments conducted in cycles of up to 2.5 MPa confining pressure. The scanning system has been used previously for similar purposes but the novel combination with a method for applying a controlled amount of stress across the fracture enabled a link to be made between the hydraulic and geometric aperture under conditions that were similar to the previous hydromechanical permeameter testing. The procedure is reasonably fast and the data analysis automated, which enables further studies with larger test series that can isolate results with statistical significance, which was beyond the

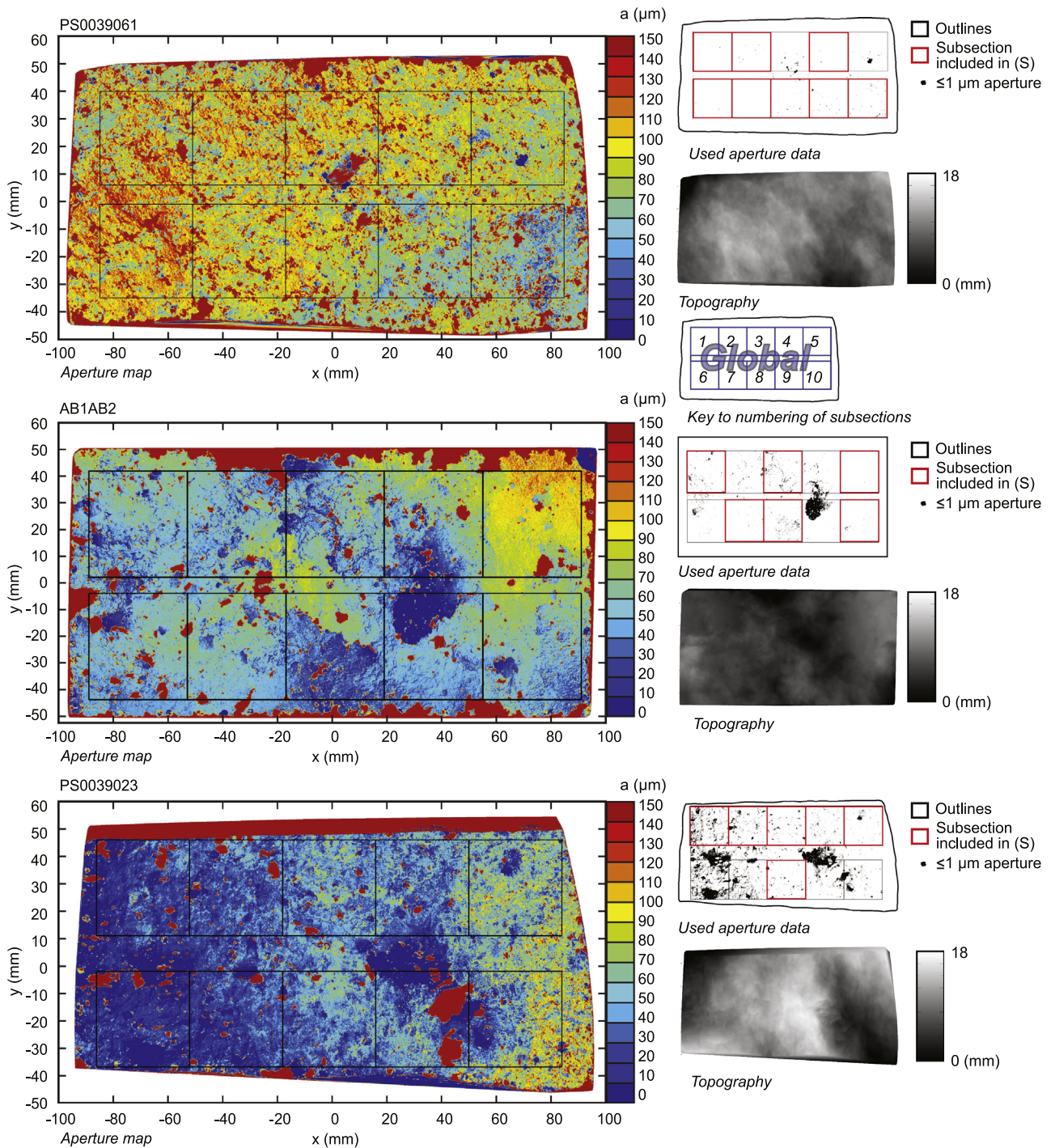


**Fig. 7.** Aperture maps of the scanned samples. The lines mark the subsections used for statistical analysis (key to numbering below the map). A small map is included, outlining which subsections were used as well as apertures below  $1 \mu\text{m}$  (contact). (For interpretation of the references to colour in this figure, the reader is referred to the web version of this article.)

scope of this initial work.

The standard deviation of the scanned aperture was high in relation to the average aperture for AB1AB2 ( $a_g = 60 \mu\text{m}$ ) and PS0039023 ( $a_g = 40 \mu\text{m}$ ), with coefficient of variation as 1.0 and 1.6, while it was lower for the sample with the largest aperture (PS0039061,  $a_g = 90 \mu\text{m}$ ); 0.6. PS0039061 had geometric mean aperture, flow-tested hydraulic aperture and topography-calculated hydraulic aperture, at similar values (93, 73–84 and 84–89  $\mu\text{m}$ ) whilst for the smallest aperture sample (PS0039023) there

was a larger difference (37, 8–9, 26). The discrepancy for PS0039023 can be attributed to some degree to the grains that fell out during the scanning procedure and the fracture being partially calcite-sealed. Correlation length was 6 mm for PS0039061 and AB1AB2, the sample with larger aperture, lower stiffness and low contact area and number of contact points. PS0039023 had a correlation length of 12 mm and a higher stiffness, lower aperture and larger contact area. These correlation length trends are also in agreement with Ref. 32.

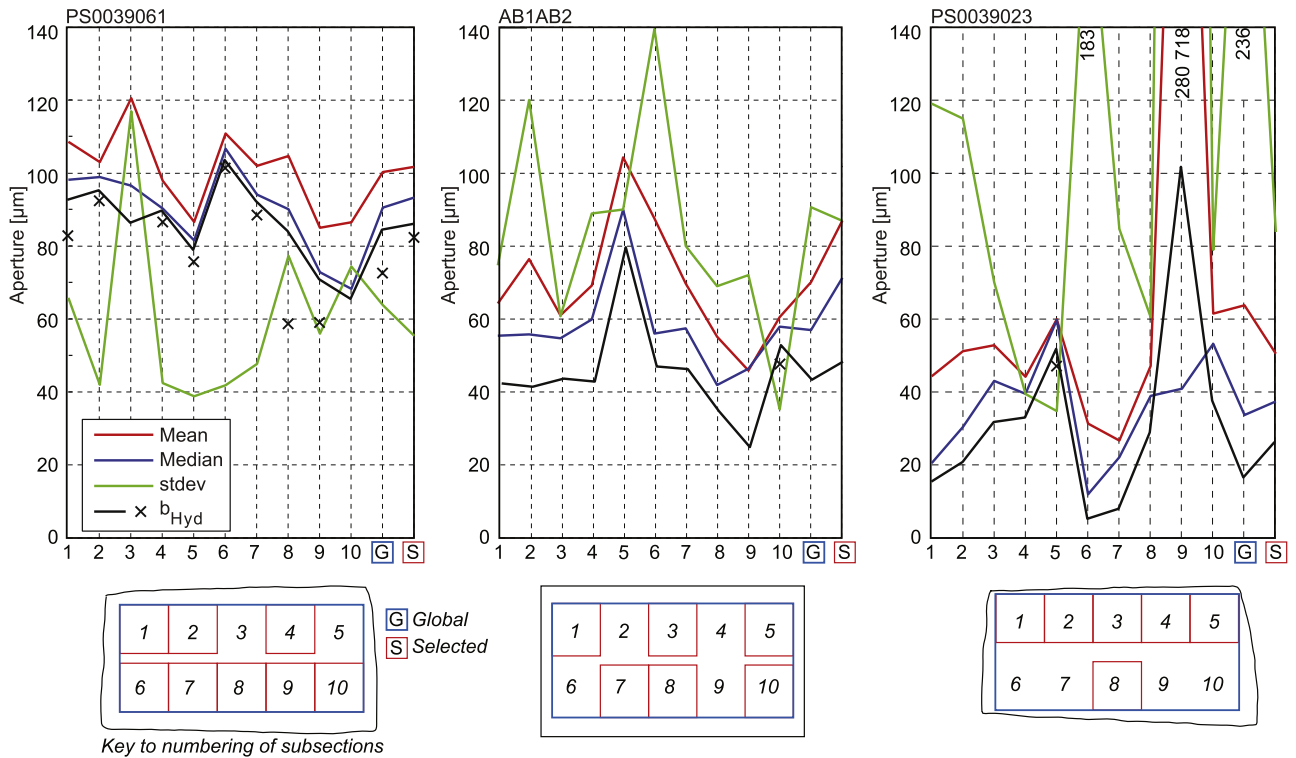


Fig. 8. Mean, median, standard deviation and hydraulic aperture for the subsections (1–10) of the three samples.

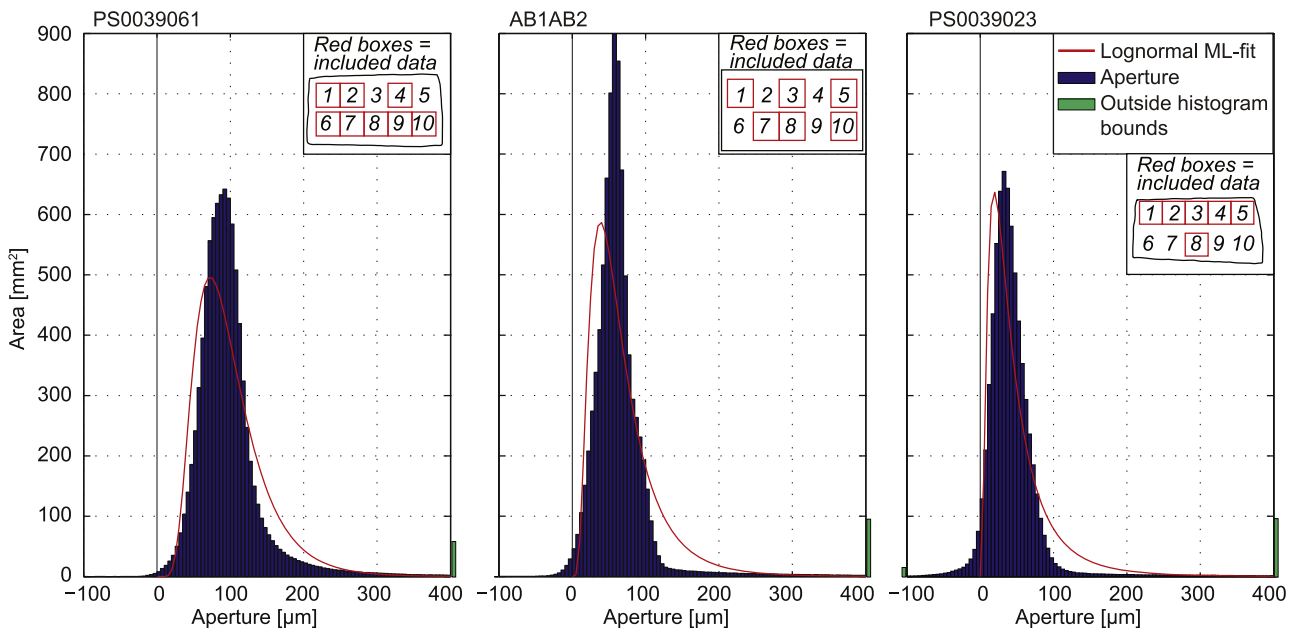


Fig. 9. Histograms of apertures of the (S) subsections. (For interpretation of the references to colour in this figure, the reader is referred to the web version of this article.)

The method and equipment allows estimates of the key parameters for a hydromechanically coupled description founded in fracture geometry: fracture hydraulic aperture and contact geometry, where the contact geometry can be expressed in terms of normal stiffness, number of contact points and correlation length of aperture. The datasets constitute a possible basis for elaborate numerical modelling of fracture deformations and coupled changes of hydraulic apertures.

Estimated hydraulic aperture and stiffness data were compared to a field data relationship of hydraulic aperture to fracture stiffness,<sup>3,7</sup> indicating that the relationship and the related conceptual model are reasonable. A fracture stiffness inversely proportional to  $b^2$  was expected for low compressional stress across fractures with limited prior deformation (e.g. crushing or shearing through of asperities), a situation similar to the setup in these investigations.

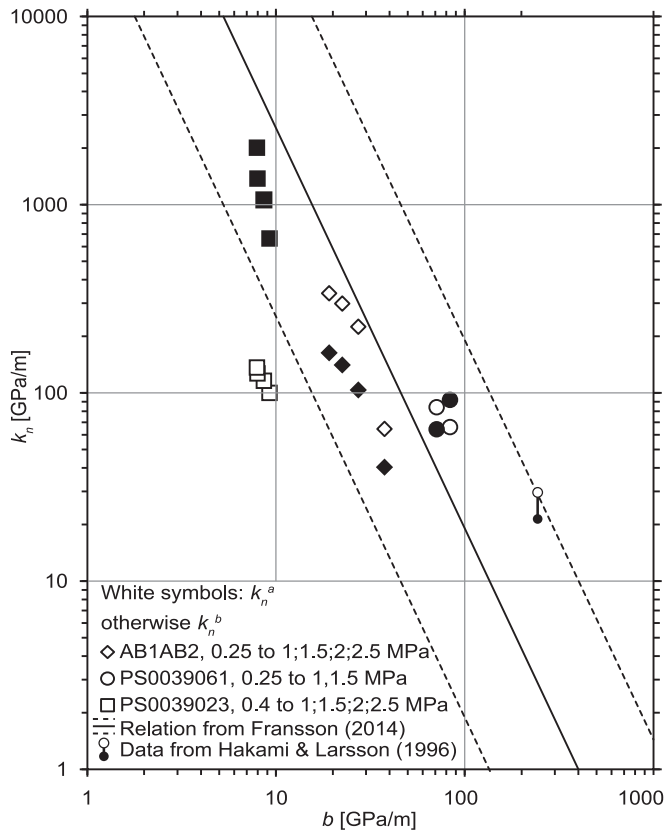


Fig. 10. Stiffness from hydromechanical tests compared to cubic law-hydraulic apertures, and in relation to Eq. (6)  $\pm$  one order of magnitude.

## Acknowledgements

The authors wish to acknowledge financial support and samples from the Swedish Nuclear Fuel and Waste Management Company, SKB. Lars O. Ericsson, for valuable discussions and work on the initial experimental set-up. Raymond Munier, SKB for fruitful discussions and encouragement. Staff at Cascade AB for running the ATOS scans. Patrick O'Malley for proofreading the manuscript and Tom Purucker, US EPA for advice on the variogram analysis.

## References

- Snow DT. Rock fracture spacings, openings and porosities. *Proc Am Soc Civil Eng*. 1968;94(SM1)73–79.
- Witherspoon PA, Wang JSY, Iwai K, Gale JE. Validity of the cubic law for fluid flow in a deformable fracture. *Water Resour Res*. 1980;16:1016–1024.
- Fransson Å. The use of basic models to explain in situ hydraulic and hydro-mechanical tests in fractured rock. *Int J Rock Mech Min Sci*. 2014;69:105–110.
- Tatone BA, Grasselli G. Quantitative measurements of fracture aperture and directional roughness from rock cores. *Rock Mech Rock Eng*. 2012;45:619–629.
- Thörn J, Ericsson L, Fransson Å. Hydraulic and hydromechanical laboratory testing of large crystalline rock cores. *Rock Mech Rock Eng*. 2014:1–13.
- Zimmerman RW, Bodvarsson GS. Hydraulic conductivity of rock fractures. *Transp Porous Media*. 1996;23:1–30.
- Fransson Å. Literature survey: relations between stress change, deformation and transmissivity for fractures and deformation zones based on in situ investigations. R-09-13. Stockholm, Sweden: Swedish Nuclear Fuel and Waste Management Co; 2009.
- Ericsson LO, Brinkhoff P, Gustafson G, Kvartsberg S. *Hydraulic features of the excavation disturbed zone—laboratory investigations of samples taken from the Q- and S-tunnels at Äspö HRL*. Stockholm, Sweden: Swedish Nuclear Fuel and Waste Management Co; 2009.
- Olsson R, Barton N. An improved model for hydromechanical coupling during shearing of rock joints. *Int J Rock Mech Min Sci*. 2001;38:317–329.
- Renshaw CE. On the relationship between mechanical and hydraulic apertures in rough-walled fractures. *J Geophys Res Solid Earth*. 1995;100:24629–24636.
- Zimmerman RW, Main I. Hydromechanical behavior of fractured rocks. In: Yves G, Maurice B, editors. *International Geophysics*. Academic Press; 2003. p. 363–421.
- Keller A. High resolution, non-destructive measurement and characterization of fracture apertures. *Int J Rock Mech Min Sci*. 1998;35:1037–1050.
- Pyrak-Nolte LJ, Myer LR, Cook NGW, Witherspoon PA. Hydraulic and mechanical properties of natural fractures in low permeability rock. In: *Proceedings of the 6th ISRM Congress*, August 30–September 3, 1987. Montreal, Canada: Balkema; 1987:255–31.
- Gale JE. *Comparison of Coupled Fracture Deformation and Fluid Flow Models With Direct Measurements of Fracture Pore Structure and Stress-flow Properties*. Tucson: Arizona; 1987.
- Johns RA, Steude JS, Castanier LM, Roberts PV. Nondestructive measurements of fracture aperture in crystalline rock cores using X ray computed tomography. *J Geophys Res Solid Earth*. 1993;98:1889–1900.
- Dagan G. Higher-order correction of effective permeability of heterogeneous isotropic formations of lognormal conductivity distribution. *Transp Porous Media*. 1993;12:279–290.
- Hakami E, Larsson E. Aperture measurements and flow experiments on a single natural fracture. *Int J Rock Mech Min Sci*. 1996;33:395–404.
- Rhén I, Forsmark T, Hartley L, et al. *Hydrogeological conceptualisation and parameterisation. Site descriptive modelling SDM—site Lexemar, R-08-78*. Stockholm, Sweden: Swedish Nuclear Fuel and Waste Management Co; 2008.
- Doe TW, Geier JE. *Interpretations of fracture system geometry using well test data. SKB stripa project TR 91-03*. Stockholm, Sweden: Swedish Nuclear Fuel and Waste Management Co; 1990.
- Ameli P, Elkhoury JE, Detwiler RL. High-resolution fracture aperture mapping using optical profilometry. *Water Resour Res*. 2013;49:7126–7132.
- Lanaro F. A random field model for surface roughness and aperture of rock fractures. *Int J Rock Mech Min Sci*. 2000;37:1195–1210.
- Gentier S, Billaux D, van Vliet L. Laboratory testing of the voids of a fracture. *Rock Mech Rock Eng*. 1989;22:149–157.
- Funehag J, Emmelin A. Injekteringen av TASS-tunneln design, genomförande och resultat från förinjekteringen, SKB R-10-39. Stockholm; 2011.
- Christiansson R, Ericsson LO, Gustafson G. Hydraulic characterisation and conceptual modelling of the Excavation Disturbed Zone (EDZ). In: *Proceedings of SINOROCK 2009 International Symposium on Rock Mechanics “Rock Characterization, Modelling and Engineering Design Methods”*. Hong Kong; 2009.
- Olsson M, Markström I, Pettersson A, Sträng M. *Examination of the excavation damaged zone in the TASS tunnel, Äspö HRL, R-09-39*. Stockholm, Sweden: Swedish Nuclear Fuel and Waste Management Co; 2009.
- Thörn J. *Coupling between changes in hydraulic and mechanical aperture: a laboratory study on rock cores. Report 2012:9*. Gothenburg, Sweden: Chalmers University of Technology; 2012.
- GOM. TRITOP-optical 3D coordinate measuring machine. url: (<http://www.gom.com/metrology-systems/large-scale-cmm.html>), Accessed 25.09.14.
- GOM. ATOS Triple scan-revolutionary scanning technique. url: (<http://www.gom.com/metrology-systems/system-overview/atos-triple-scan.html>), Accessed 25.09.14.
- Thörn J, Fransson Å. *Fracture aperture measurement and consequences for grouting*. In: *Proceedings of the 7th Nordic Grouting Symposium*. Gothenburg, Sweden: BeFo; 2013. p. 183–193.
- GOM. GOM inspect. url: (<http://www.gom.com/3d-software/gom-inspect.html>), Accessed 25.09.14.
- Mathworks. Matlab r2012b.
- Hakami E. *Aperture Distribution of Rock Fractures* [Ph.D. thesis]. Stockholm, Sweden: Royal Institute of Technology; 1995.
- Hakami E, Einstein HH, Gentier S, Iwano M. *Characterisation of fracture apertures—methods and parameters*. International Society for Rock Mechanics.
- Larsson E. *Groundwater Flow Through a Natural Fracture—flow Experiments and Numerical Modelling*. Gothenburg: Chalmers University of Technology; 1997.
- Thörn J, Fransson Å. *Fracture Aperture Measurement and Consequences for Grouting*. Gothenburg, Sweden: BeFo-Swedish Rock Engineering Research Foundation; 2013.